# New Steady State Current Error Limiters for PMSM Drives

Hemantha Kumar RAVI [iD] , Lenin NATESAN CHOKKALINGAM *[iD]

*Electric Vehicles – Incubation, Testing, and Research Center, School of Electrical Engineering, Vellore Institute of Technology (VIT) University, Chennai, India*

**Highlights**
• New FOC principle-based scheme for the PMSM drive.
• Two control structure for the PMSM drive control has been proposed and results are discussed briefly.
• Thermal analysis on the inverter due to proposed schemes.

**Abstract**

In permanent magnet synchronous motor drives, d-q current errors are examined using hysteresis controllers. The inverter is switched based on the hysteresis controller responses, to limit current errors, thereby reducing current ripple. But, due to the faster current dynamic characteristics, switching the current errors within the hysteresis band becomes difficult. This results in d-q current ripples and harmonics. In this paper, two current error-limiting schemes are proposed. In the first scheme, current errors are switched within the band using additional control parameters (dynamic response of q-axis current), to select the control space vector from a switching table. Whereas in the second scheme, a duty ratio regulator is designed to achieve minimum q-axis current error. The proposed works are simulated in MATLAB/Simulink and verified through experimentation. Since the current ripple and harmonics are also reduced, the thermal impact of these performance parameters on the power inverter is also studied.

## 1. INTRODUCTION

A permanent magnet synchronous motor (PMSM) is known for its high-power density and efficiency [1, 2]. PMSM drives are controlled widely using either direct torque control (DTC) or field-oriented control (FOC) schemes [3, 4]. DTC has a simple control structure (with hysteresis band and switching table) for decoupling stator flux and electromagnetic torque (as shown in Figure 1) [5-7].
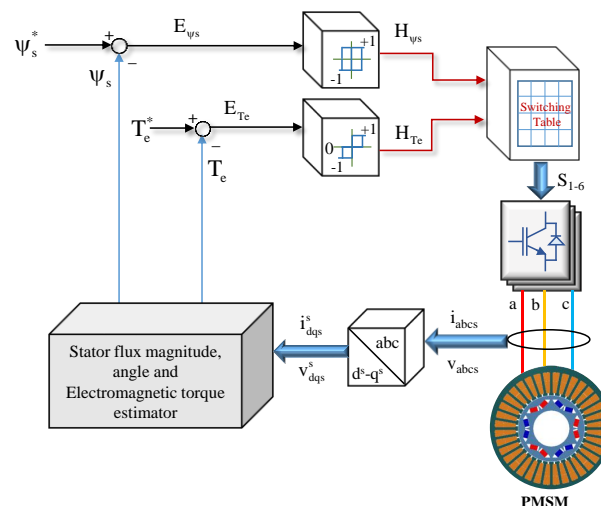


*Figure 1. Control structure of the DTC scheme*

*Corresponding author, e-mail: lenin.nc@vit.ac.in

The major advantage of the DTC-based PMSM drive is the high dynamic torque response. Whereas the structure of DTC results in high torque ripple and current harmonics [8-10]. In the FOC-based PMSM drive, stator d-q current components are regulated to achieve decoupled control of torque and rotor flux (as shown in Figure 2) [11, 12]. The direct current regulation in FOC leads to lower current harmonics than in DTC [8]. During current regulation, FOC also suffers from current ripples and unbalanced conditions, while switching the phase current errors [13, 14]. To improve the current regulation in FOC, various current regulation strategies have been discussed in the literature [15- 58].
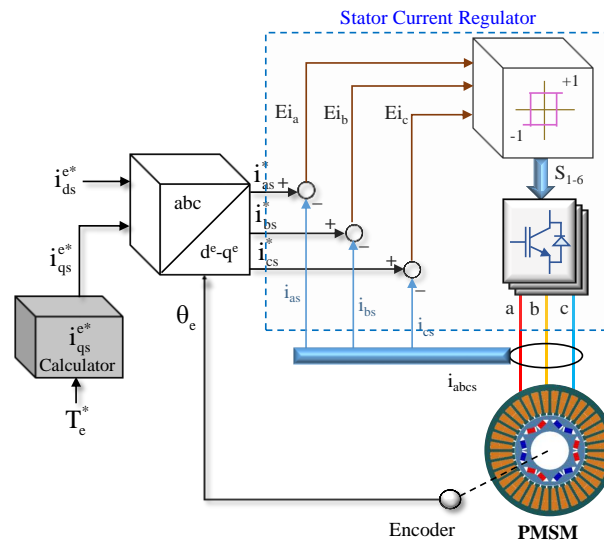


*Figure 2. Block diagram of the field-oriented control scheme*
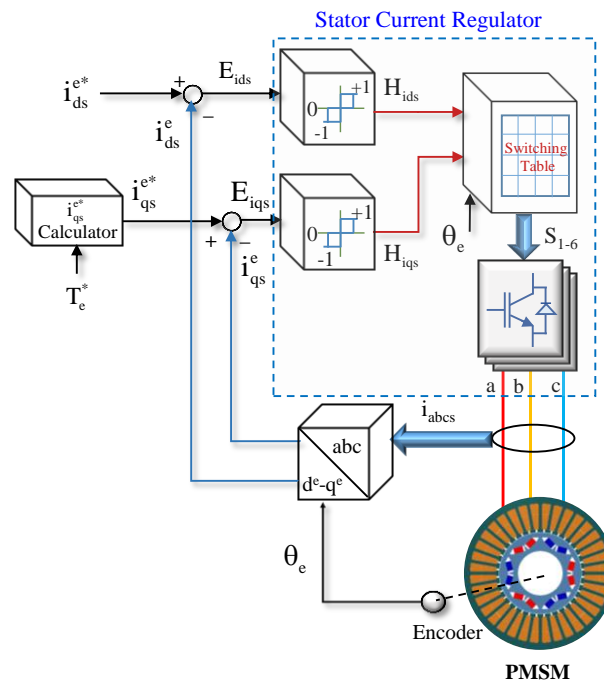


*Figure 3. Block diagram of the hybrid torque and flux control scheme*

The current regulation strategies for FOC can be classified into linear and non-linear current regulators [13]. Linear current regulators utilize conventional pulse width modulators (PWM) such as sinusoidal PWM, space vector PWM etc., for current regulation. Nonlinear current regulation strategies can be categorized as hysteresis controllers [17, 18, 38–45], online optimal controllers [46–50] and soft-computing

controllers [51–68]. Due to the presence of PWM controllers, linear current regulators provide better performance than non-linear controllers, which includes constant switching frequency, current characteristics (lower ripple and harmonics), lower torque ripple and good DC-link utilization [13]. But nonlinear controllers provide good error tracking, and simple and robust control compared to linear controllers [1, 2, 14].

Among non-linear current regulation strategies, space vector-based FOC schemes are preferred because of their constant switching frequency, balanced phase currents, linear current control characteristics, and good DC-link voltage utilization [17-19]. In the early 1990s, Kazmierkowski et al. introduced a hysteresis controller and switching table-based FOC control scheme [17-18]. The switching table has been designed to provide space vectors for the inverter control based on the hysteresis controller output as shown in Figure 3. This control structure is like the DTC control structure in Figure 1. Thus, this scheme can also be known as the hybrid torque and flux control (HTFC) scheme. This scheme results in d-q current ripples, because of the inaccurate switching of the control voltage vector, based on the d-q current error condition within the hysteresis band [18].

In this paper, HTFC-based PMSM drive performance is analyzed and improved HTFC schemes are proposed. The objective of the proposed schemes is to limit the current component errors, such that current ripples and harmonics are reduced as well. Since these characteristics influence the inverter losses, the thermal impact of the discussed HTFC schemes is also studied.

## 2. HYBRID TORQUE AND FLUX CONTROL SCHEME

### 2.1. Control Principle

The HTFC scheme works on the principle of the FOC scheme. PMSM can be modelled as follows [2],

$$\begin{bmatrix} v_{qs}^e \\ v_{ds}^e \end{bmatrix} = \begin{bmatrix} R_s + L_q\rho & \omega_e L_d \\ -\omega_e L_q & R_s + L_d\rho \end{bmatrix} \begin{bmatrix} i_{qs}^e \\ i_{ds}^e \end{bmatrix} + \begin{bmatrix} \omega_e \psi_f \\ 0 \end{bmatrix} \tag{1}$$

$$\psi_{qs}^e = L_q i_{qs}^e \tag{2}$$

$$\psi_{ds}^e = L_d i_{ds}^e + \psi_f \tag{3}$$

$$T_e = \frac{3}{2}\left(\frac{P}{2}\right)(\psi_s \times I_s) = \frac{3}{2}\left(\frac{P}{2}\right)\left(\psi_{ds}^e i_{qs}^e - \psi_{qs}^e i_{ds}^e\right) \quad . \tag{4}$$

The stator phase currents can also be expressed in terms of load angle and synchronous speed as,

$$i_{as} = I_s \sin\left(\omega_e t + \delta\right) \tag{5}$$

$$i_{bs} = I_s \sin\left(\omega_e t + \delta - \frac{2\pi}{3}\right) \tag{6}$$

$$i_{cs} = I_s \sin\left(\omega_e t + \delta + \frac{2\pi}{3}\right) \quad . \tag{7}$$

Park's transformation equation for the stator phase currents is

$$
\begin{bmatrix} i_{qs}^e \\ i_{ds}^e \end{bmatrix} = \frac{2}{3} \begin{bmatrix} \cos\theta_e & \cos\left(\theta_e - \dfrac{2\pi}{3}\right) & \cos\left(\theta_e + \dfrac{2\pi}{3}\right) \\[2mm] \sin\theta_e & \sin\left(\theta_e - \dfrac{2\pi}{3}\right) & \sin\left(\theta_e + \dfrac{2\pi}{3}\right) \end{bmatrix} \begin{bmatrix} i_{as} \\ i_{bs} \\ i_{cs} \end{bmatrix} .
$$

(8)

On substituting (5-7) in (8),

$$
\begin{bmatrix} i_{qs}^e \\ i_{ds}^e \end{bmatrix} = I_s \begin{bmatrix} \sin\delta \\ \cos\delta \end{bmatrix} .
$$

(9)

Since $\delta$ is a constant for given load torque, the d-q axes currents are constants in the synchronous reference frame. From stator flux Equations (2-3), electromagnetic torque Equation (4) can be rewritten as,

$$
T_e = \frac{3}{2}\left(\frac{P}{2}\right)\left(\psi_{ds}^e i_{qs}^e - \psi_{qs}^e i_{ds}^e\right) = \frac{3}{2}\left(\frac{P}{2}\right)\left(\left(L_d i_{ds}^e + \psi_f\right)i_{qs}^e - \left(L_q i_{qs}^e\right)i_{ds}^e\right)
$$

(10)

$$
T_e = \frac{3}{2}\left(\frac{P}{2}\right)\left(L_d i_{ds}^e i_{qs}^e + \psi_f i_{qs}^e - L_q i_{qs}^e i_{ds}^e\right) .
$$

(11)

On substituting, the d-q axes stator currents in (9),

$$
T_e = \frac{3}{2}\left(\frac{P}{2}\right)\left(L_d I_s^2 \sin\delta\cos\delta + \psi_f I_s \sin\delta - L_q I_s^2 \sin\delta\cos\delta\right)
$$

(12)

$$
T_e = \frac{3}{2}\left(\frac{P}{2}\right)\left(L_d I_s^2 \frac{\sin 2\delta}{2} + \psi_f I_s \sin\delta - L_q I_s^2 \frac{\sin 2\delta}{2}\right)
$$

(13)

$$
T_e = \frac{3}{2}\left(\frac{P}{2}\right)\left(\frac{1}{2}\left(L_d - L_q\right)I_s^2 \frac{\sin 2\delta}{2} + \psi_f I_s \sin\delta\right) .
$$

(14)

In the electromagnetic torque Equation (14), $L_d \leq L_q$ and thus, the first torque component (reluctance) is positive only if $i_{ds}^e \leq 0$. For $i_{ds}^e < 0$, the permanent magnet flux is reduced. Thus, the $i_{ds}^e$ current is taken as zero in FOC for PMSM during constant torque operation. This means that the electromagnetic torque in PMSM can be controlled by controlling the q-axis stator current and the stator current is aligned with q$^e$-axis.

## 2.2. Control Block Diagram

In the HTFC-based PMSM drive (shown in Figure 3), the reference $i_{qs}^e$ current is calculated from the command torque using Equation (15). From Equation (14),

$$
i_{qs}^{e*} = \frac{T_e^*}{\dfrac{3}{2}\left(\dfrac{P}{2}\right)\psi_f} \qquad \left(\because I_s = i_{qs}^e \quad and \quad \delta = \frac{\pi}{2}\right) .
$$

(15)

***Table 1.*** *Switching table of the HTFC-PMSM drive*

| | $H_{ids}$ | 1 | | | 0 | | | -1 | | |
|---|---|---|---|---|---|---|---|---|---|---|
| | $H_{iqs}$ | 1 | 0 | -1 | 1 | 0 | -1 | 1 | 0 | -1 |
| | $S_1$ | $V_2$ | $V_1$ | $V_6$ | $V_3$ | $V_0$ | $V_6$ | $V_3$ | $V_4$ | $V_5$ |
| | $S_2$ | $V_2$ | $V_1$ | $V_1$ | $V_3$ | $V_0$ | $V_6$ | $V_4$ | $V_4$ | $V_5$ |
| | $S_3$ | $V_2$ | $V_2$ | $V_1$ | $V_3$ | $V_0$ | $V_6$ | $V_4$ | $V_5$ | $V_5$ |
| | $S_4$ | $V_3$ | $V_2$ | $V_1$ | $V_3$ | $V_0$ | $V_6$ | $V_4$ | $V_5$ | $V_6$ |
| | $S_5$ | $V_3$ | $V_2$ | $V_1$ | $V_4$ | $V_0$ | $V_1$ | $V_4$ | $V_5$ | $V_6$ |
| | $S_6$ | $V_3$ | $V_2$ | $V_2$ | $V_4$ | $V_0$ | $V_1$ | $V_5$ | $V_5$ | $V_6$ |
| | $S_7$ | $V_3$ | $V_3$ | $V_2$ | $V_4$ | $V_0$ | $V_1$ | $V_5$ | $V_6$ | $V_6$ |
| | $S_8$ | $V_4$ | $V_3$ | $V_2$ | $V_4$ | $V_0$ | $V_1$ | $V_5$ | $V_6$ | $V_1$ |
| | $S_9$ | $V_4$ | $V_3$ | $V_2$ | $V_5$ | $V_0$ | $V_2$ | $V_5$ | $V_6$ | $V_1$ |
| Sectors | $S_{10}$ | $V_4$ | $V_3$ | $V_3$ | $V_5$ | $V_0$ | $V_2$ | $V_6$ | $V_6$ | $V_1$ |
| | $S_{11}$ | $V_4$ | $V_4$ | $V_3$ | $V_5$ | $V_0$ | $V_2$ | $V_6$ | $V_1$ | $V_1$ |
| | $S_{12}$ | $V_5$ | $V_4$ | $V_3$ | $V_5$ | $V_0$ | $V_2$ | $V_6$ | $V_1$ | $V_2$ |
| | $S_{13}$ | $V_5$ | $V_4$ | $V_3$ | $V_6$ | $V_0$ | $V_3$ | $V_6$ | $V_1$ | $V_2$ |
| | $S_{14}$ | $V_5$ | $V_4$ | $V_4$ | $V_6$ | $V_0$ | $V_3$ | $V_1$ | $V_1$ | $V_2$ |
| | $S_{15}$ | $V_5$ | $V_5$ | $V_4$ | $V_6$ | $V_0$ | $V_3$ | $V_1$ | $V_2$ | $V_2$ |
| | $S_{16}$ | $V_6$ | $V_5$ | $V_4$ | $V_6$ | $V_0$ | $V_3$ | $V_1$ | $V_2$ | $V_3$ |
| | $S_{17}$ | $V_6$ | $V_5$ | $V_4$ | $V_1$ | $V_0$ | $V_4$ | $V_1$ | $V_2$ | $V_3$ |
| | $S_{18}$ | $V_6$ | $V_5$ | $V_5$ | $V_1$ | $V_0$ | $V_4$ | $V_2$ | $V_2$ | $V_3$ |
| | $S_{19}$ | $V_6$ | $V_6$ | $V_5$ | $V_1$ | $V_0$ | $V_4$ | $V_2$ | $V_3$ | $V_3$ |
| | $S_{20}$ | $V_1$ | $V_6$ | $V_5$ | $V_1$ | $V_0$ | $V_4$ | $V_2$ | $V_3$ | $V_4$ |
| | $S_{21}$ | $V_1$ | $V_6$ | $V_5$ | $V_2$ | $V_0$ | $V_5$ | $V_2$ | $V_3$ | $V_4$ |
| | $S_{22}$ | $V_1$ | $V_6$ | $V_6$ | $V_2$ | $V_0$ | $V_5$ | $V_3$ | $V_3$ | $V_4$ |
| | $S_{23}$ | $V_1$ | $V_1$ | $V_6$ | $V_2$ | $V_0$ | $V_5$ | $V_3$ | $V_4$ | $V_4$ |
| | $S_{24}$ | $V_2$ | $V_1$ | $V_6$ | $V_2$ | $V_0$ | $V_5$ | $V_3$ | $V_4$ | $V_5$ |

In a synchronous reference frame, the phase currents are transformed into d-q current components ($i_{ds}^e$ and $i_{qs}^e$) and compared with the corresponding reference currents ($i_{ds}^{e*}$ and $i_{qs}^{e*}$). The current errors ($\Delta i_{ds}^e$ and $\Delta i_{qs}^e$) are examined using 3-level hysteresis controllers, whose outputs are given in Equations (16-17).

$\Delta i_{ds}^e$ hysteresis band output,

$$H_{ids} = \begin{cases} 1 & for \quad E_{ids} > +HB_{ids} \\ 0 & for \quad -HB_{ids} < E_{ids} < +HB_{ids} \\ -1 & for \quad E_{ids} < -HB_{ids} \end{cases}$$

(16)

$\Delta i_{qs}^{e}$ hysteresis band output,

$$H_{iqs} = \begin{cases} 1 & for & E_{iqs} > +HB_{iqs} \\ 0 & for & -HB_{iqs} < E_{iqs} < +HB_{iqs} \\ -1 & for & E_{iqs} < -HB_{iqs} \end{cases} \quad .$$
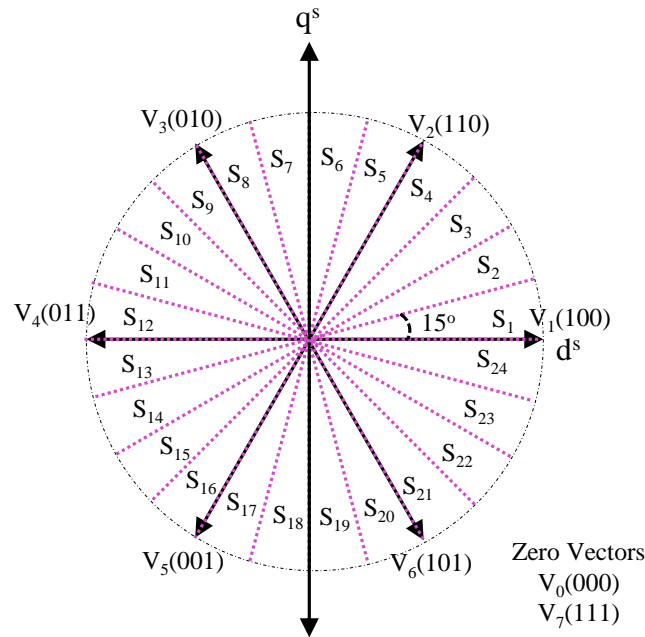
$(17)$



**Figure 4.** *Active voltage vectors in the control space*

The hysteresis controller outputs and the electrical rotor angle generate the required space voltage vector using a switching table (as in Table 1). The d-q axes currents move in the direction of the applied space voltage vector. The control voltage space vectors (refer Figure 4) are placed in the switching table, such that the d-q current errors are limited.

## 3. PROPOSED SCHEME 1 – MUTATED SWITCHING TABLE (MST) SCHEME

In the conventional HTFC scheme, d-q axes stator current errors are controlled by applying six active voltage vectors. When the active voltage vector is applied, the dynamic response of the current errors is maximum. This makes switching at the instant when the current errors reach any level of the hysteresis band, a challenge.

To assure appropriate switching, the MST scheme proposes a 4-level hysteresis band for the $i_{qs}^{e}$ current error (+2,+1,-1,-2) and a 2-level hysteresis band (+1,-1) for the $i_{ds}^{e}$ error. In the 4-level controller, an intermediary control voltage is applied to reduce the dynamics of the $i_{qs}^{e}$ current error at the hysteresis level of (+1,-1). This reduces the response (rate of change) of the $i_{qs}^{e}$ current and ensures switching at the outer boundary of the 4-level hysteresis band (+2,-2). The application of the zero-voltage vector reduces the stator flux. To avoid a zero-voltage vector, the zero hysteresis levels are skipped in both d-axis and q-axis hysteresis bands.
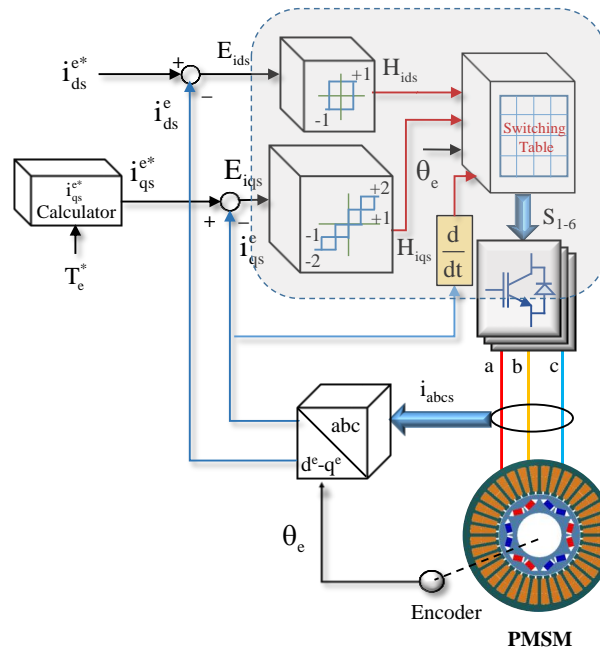
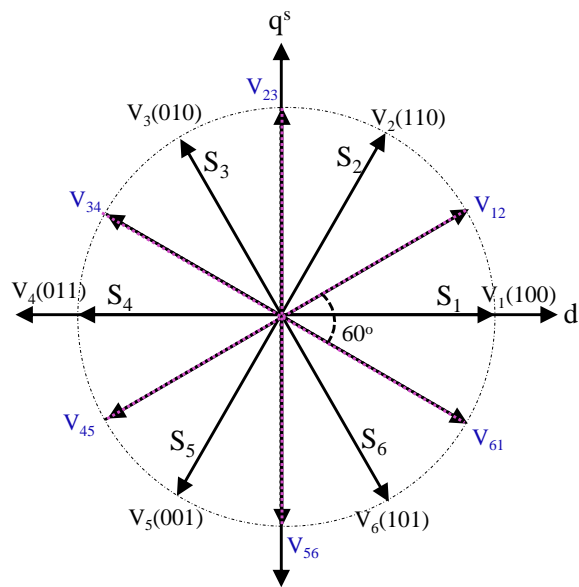**Figure 5.** *Block diagram of the MST scheme-based PMSM drive*



**Figure 6.** *Active and intermediary voltage vectors in control space*

The MST-based PMSM drive is shown in Figure 5. Using the intermediary voltage vectors, a switching table (refer to Table 2) is formulated. It can be observed from Figure 5 and Table 2 that an additional parameter (the sign of the rate of change of $i_{qs}^e$ current) for control voltage vector selection is incorporated. This parameter is used to avoid inappropriate switching at the (+1,-1) levels of the $i_{qs}^e$ current error hysteresis band. For example, assume the sign of the rate change of the $i_{qs}^e$ current is negative. This means that the slope of the current error is positive in the hysteresis band. The current error is required to be switched at the +1 hysteresis level, such that its dynamic response is slowed down before reaching the +2 hysteresis level. Thus, based on the sign of the rate change of the $i_{qs}^e$ current, the switching of the $i_{qs}^e$ current error at the -1 level is avoided.

The space vector representation for the switching table (refer to Table 2) is shown in Figure 6. At a 50% duty ratio, bounding active voltage vectors are switched to generate the intermediary voltage vectors.

***Table 2.** MST-Scheme-switching table*

| $H_{ids}$ | $\dfrac{di_{qs}^e}{dt}$ | $H_{iqs}$ | Sectors | | | | | |
|---|---|---|---|---|---|---|---|---|
| | | | $S_1$ | $S_2$ | $S_3$ | $S_4$ | $S_5$ | $S_6$ |
| +1 | Positive | +2 | $V_2$ | $V_3$ | $V_4$ | $V_5$ | $V_6$ | $V_1$ |
| | | +1 | $V_2$ | $V_3$ | $V_4$ | $V_5$ | $V_6$ | $V_1$ |
| | | -1 | $V_{12}$ | $V_{23}$ | $V_{34}$ | $V_{45}$ | $V_{56}$ | $V_{61}$ |
| | | -2 | $V_6$ | $V_1$ | $V_2$ | $V_3$ | $V_4$ | $V_5$ |
| | Negative | +2 | $V_2$ | $V_3$ | $V_4$ | $V_5$ | $V_6$ | $V_1$ |
| | | +1 | $V_{61}$ | $V_{12}$ | $V_{23}$ | $V_{34}$ | $V_{45}$ | $V_{56}$ |
| | | -1 | $V_6$ | $V_1$ | $V_2$ | $V_3$ | $V_4$ | $V_5$ |
| | | -2 | $V_6$ | $V_1$ | $V_2$ | $V_3$ | $V_4$ | $V_5$ |
| -1 | Positive | +2 | $V_3$ | $V_4$ | $V_5$ | $V_6$ | $V_1$ | $V_2$ |
| | | +1 | $V_3$ | $V_4$ | $V_5$ | $V_6$ | $V_1$ | $V_2$ |
| | | -1 | $V_{34}$ | $V_{45}$ | $V_{56}$ | $V_{61}$ | $V_{12}$ | $V_{23}$ |
| | | -2 | $V_5$ | $V_6$ | $V_1$ | $V_2$ | $V_3$ | $V_4$ |
| | Negative | +2 | $V_3$ | $V_4$ | $V_5$ | $V_6$ | $V_1$ | $V_2$ |
| | | +1 | $V_{45}$ | $V_{56}$ | $V_{61}$ | $V_{12}$ | $V_{23}$ | $V_{34}$ |
| | | -1 | $V_5$ | $V_6$ | $V_1$ | $V_2$ | $V_3$ | $V_4$ |
| | | -2 | $V_5$ | $V_6$ | $V_1$ | $V_2$ | $V_3$ | $V_4$ |

## 4. PROPOSED SCHEME 1 – MUTATED SWITCHING TABLE (MST) SCHEME

The objective of the DRM scheme is to find the duty ratio of the control vector, such that the RMS current ripple is minimum in control sampling time ($t_{cs}$). This optimal duty ratio is estimated from the dynamic response of the $i_{qs}^e$ current and the RMS current ripple. The RMS $i_{qs}^e$ current ripple over a control sampling time ($t_{cs}$) can be expressed as,

$$i_{qs(ripple)}^e = \sqrt{\frac{1}{t_{cs}}\int_0^{t_{cs}}\left(i_{qs(error)}^e\right)^2 dt} = \sqrt{\frac{1}{t_{cs}}\int_0^{t_{cs}}\left(i_{qs}^e - i_{qs}^{e*}\right)^2 dt} \quad .$$

(18)

For instance, assume an active voltage vector is applied, and the $i_{qs}^e$ current increases with a slope of $S_1$ (as shown in Figure 7) in time *0-t_s*. Then, a zero-voltage vector is applied. This reduces the $i_{qs}^e$ current in time $t_{cs}$-$t_s$ (negative slope, $S_2$). If $i_{qso}^e$ is the initial $i_{qs}^e$ current, the positive and negative slope intervals (from Figure 7) can be expressed as,

$$i_{qs}^e = \begin{cases} i_{qso}^e + k_1 t, & 0 \le t \le t_s \\ i_{qso}^e + k_1 t_s + k_2 t - k_2 t_s, & t_s \le t \le t_{cs} \end{cases} \quad .$$

(19)

Using (19), (18) can be expanded as,

$$i_{qs(ripple)}^{e} = \sqrt{\frac{1}{t_{cs}}\left[\int_{0}^{t_{s}}\left(i_{qso}^{e} + k_{1}t - i_{qso}^{e*}\right)^{2} dt\right]} + \sqrt{\frac{1}{t_{cs}}\left[\int_{t_{s}}^{t_{cs}}\left(i_{qso}^{e} + k_{1}t_{s} + k_{2}t - k_{2}t_{s} - i_{qso}^{e*}\right)^{2} dt\right]} \quad .$$
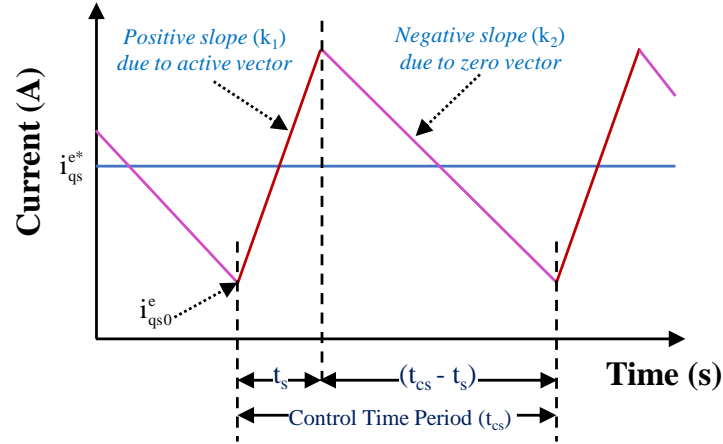
(20)



**Figure 7.** *q-axis current dynamics over the control sampling time, $t_{cs}$*

From the calculus maxima and minima principle, the following condition needs to be satisfied to achieve minimum $i_{qs}^{e}$ ripple,

$$\frac{\partial i_{qs(ripple)}^{e}}{\partial t_{s}} = 0 \quad .$$

(21)

Thus, a relationship between the RMS $i_{qs}^{e}$ current ripple and the minimum ripple condition can be established by solving Equations (20)-(21) [26]. Therefore,

$$\frac{\partial i_{qs(ripple)}^{e}}{\partial t_{s}} = \sqrt{-\frac{\left(k_{1} - k_{2}\right)}{t_{cs}}\left[\left(2k_{1} - k_{2}\right)t_{s}^{2} + 2\left(i_{qso}^{e} - i_{qs}^{e*} - \left(k_{1} - k_{2}\right)t_{cs}\right)t_{s} - \left(2\left(i_{qso}^{e} - i_{qs}^{e*}\right)t_{cs} + k_{2}t_{cs}^{2}\right)\right]} \quad .$$

(22)

The optimal active vector switching time ($t_s$) is calculated from (22) [59]

$$t_{s} = \frac{2\left(i_{qs}^{e*} - i_{qso}^{e}\right) - k_{2}t_{cs}}{2k_{1} - k_{2}} \quad .$$

(23)

To solve the above equation, first, the dynamic response of the $i_{qs}^{e}$ current during positive slope and negative slope (S$_1$ and S$_2$) should be known.

From the stator q-axis voltage Equation (1),

$$v_{qs}^{e} = R_{s}i_{qs}^{e} + L_{q}\rho i_{qs}^{e} + \omega_{e}L_{d}i_{ds}^{e} + \omega_{e}\psi_{f} \quad .$$

(24)

On rearranging,

$$\rho i_{qs}^{e} = \frac{v_{qs}^{e} - R_s i_{qs}^{e} - \omega_e L_d i_{ds}^{e} - \omega_e \psi_f}{L_q} \quad .$$

$$(25)$$

For a small sampling period $t_{sp}$, (25) can be represented as,

$$\rho i_{qs}^{e} = \frac{\Delta i_{qs}^{e}}{t_{sp}} = \frac{v_{qs}^{e} - R_s i_{qs}^{e} - \omega_e L_d i_{ds}^{e} - \omega_e \psi_f}{L_q} \quad .$$

$$(26)$$

When the zero-voltage vector is applied $i_{qs}^{e}$ current becomes zero, thus the positive and negative slopes are deduced from (26) as,

$$k_1 = \frac{\Delta i_{qs}^{e}}{t_{sp}} = \frac{v_{qs}^{e} - R_s i_{qs}^{e} - \omega_e L_d i_{ds}^{e} - \omega_e \psi_f}{L_q}$$

$$(27)$$

$$k_2 = \frac{\Delta i_{qs}^{e}}{t_{sp}} = \frac{-R_s i_{qs}^{e} - \omega_e L_d i_{ds}^{e} - \omega_e \psi_f}{L_q} \quad .$$

$$(28)$$

From (27)- (28), the optimal duty ratio can be calculated using (23) in the duty ratio modulation block of the proposed DRM scheme as shown in Figure 8. The implementation flow chart of this block is presented in Figure 9. In this scheme, two-level hysteresis controllers are used as $i_{ds}^{e}$ and $i_{qs}^{e}$ current error controllers. The space vector representation of the control voltage vectors and the switching table for this scheme are given in Figure 10 and Table 3 respectively.
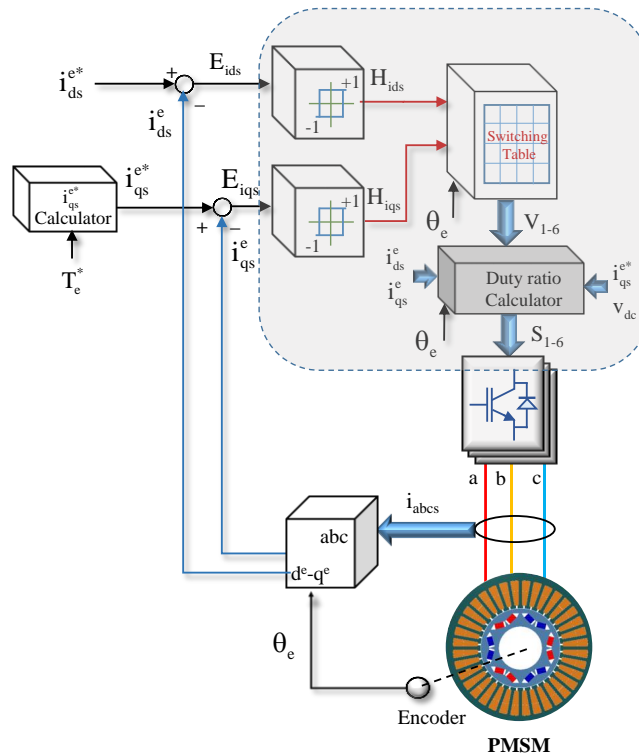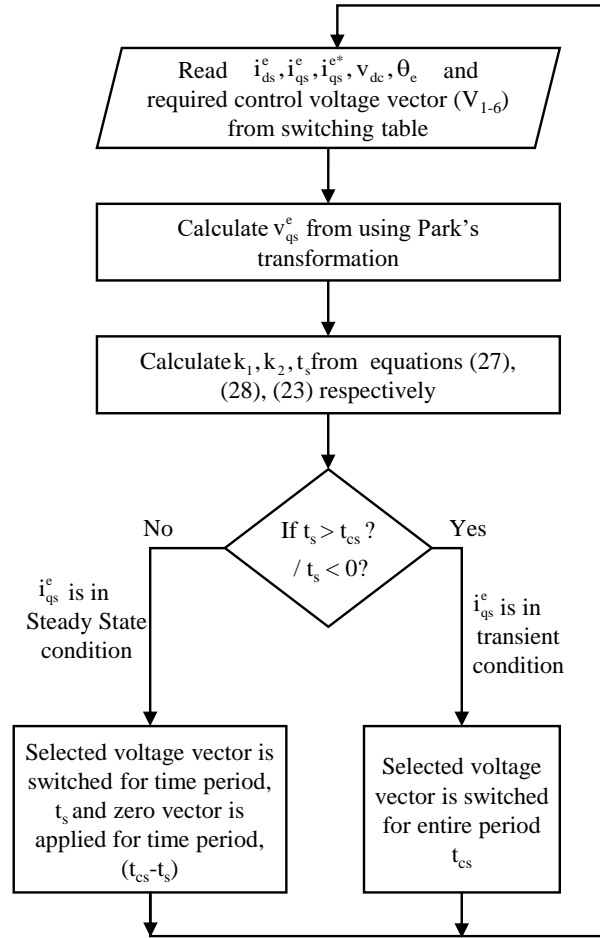


*Figure 8. Block diagram of the DRM scheme*

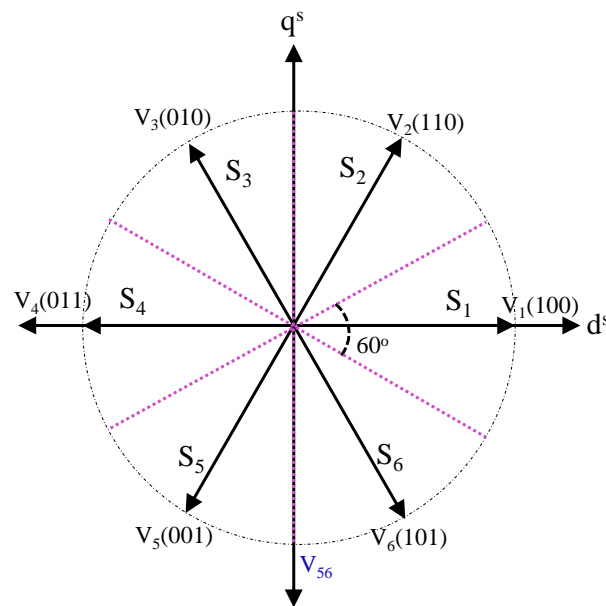**Figure 9.** *Implementation flowchart of the duty-ratio calculator block*



**Figure 10.** *Active voltage vectors in control space with 6-sectors*

**Table 3.** *Switching table of the DRM scheme*

| $H_{ids}$ | $H_{iqs}$ | Sectors | | | | | |
|---|---|---|---|---|---|---|---|
| | | $S_1$ | $S_2$ | $S_3$ | $S_4$ | $S_5$ | $S_6$ |
| +1 | +1 | $V_2$ | $V_3$ | $V_4$ | $V_5$ | $V_6$ | $V_1$ |
| | -1 | $V_6$ | $V_1$ | $V_2$ | $V_3$ | $V_4$ | $V_5$ |
| -1 | +1 | $V_3$ | $V_4$ | $V_5$ | $V_6$ | $V_1$ | $V_2$ |
| | -1 | $V_5$ | $V_6$ | $V_1$ | $V_2$ | $V_3$ | $V_4$ |

## 5. RESULTS AND DISCUSSION

The parameters of the 1kW three-phase test PMSM are tabulated in Table 4. The conventional HTFC and proposed (MST and DRM) schemes are simulated and verified in experimentation. The fundamental sampling time is 10μs. The $i_{ds}^e$ and $i_{qs}^e$ error control hysteresis bandwidth is 0.05 A.

**Table 4.** *1kW, 3-Phase PMSM drive*

| Nameplate details/Parameters | Values |
|---|---|
| Voltage | 220 Vac |
| Speed | 4600 rpm |
| No. of pole pairs | 3 |
| Rotor magnet flux | 0.16 Wb |
| Stator phase resistance | 2.05 Ω |
| Stator phase inductance | 6.68 mH |
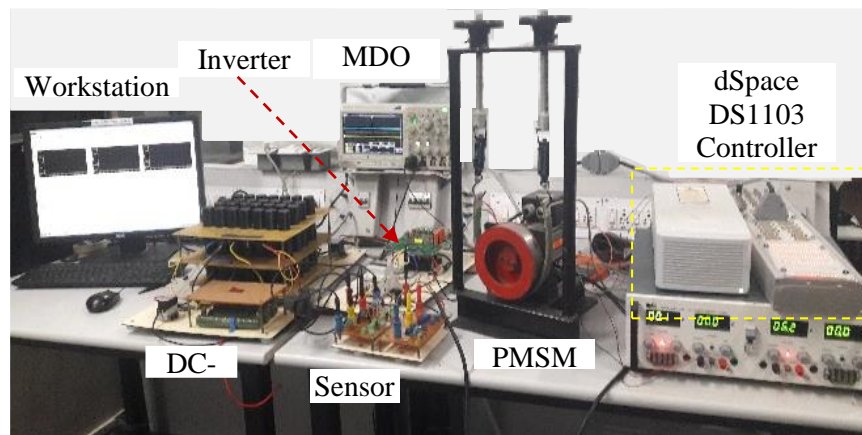


**Figure 11.** *Experimental test setup*

In the experimental setup (shown in Figure 11), conventional and proposed schemes are programmed in the dSpace 1103 controller, and the generated control pulses are given to the inverter drive. The three-phase inverter circuit is designed using an intelligent power module (FSBB20CH60). The inverter dead time is 2.5μs. The inverter phase currents are measured using an ACS712 bidirectional sensor. For loading the PMSM drive, it is coupled with the brake drum.

### 5.1. HTFC Scheme

The drive speed of the PMSM drive is set at 4600 rpm and the drive performance observed during simulation and experimentation is presented in Figures 12 and 13, respectively. At 1s, a load of 2Nm is applied to the motor. The $i_{ds}^e$ and $i_{qs}^e$ currents are controlled using three-level hysteresis controllers. The inverter switching error at the appropriate level of the hysteresis band cause ripples in the d-q axes currents. The $i_{ds}^e$ and $i_{qs}^e$ current errors are observed to be 0.23A and 0.28A respectively.
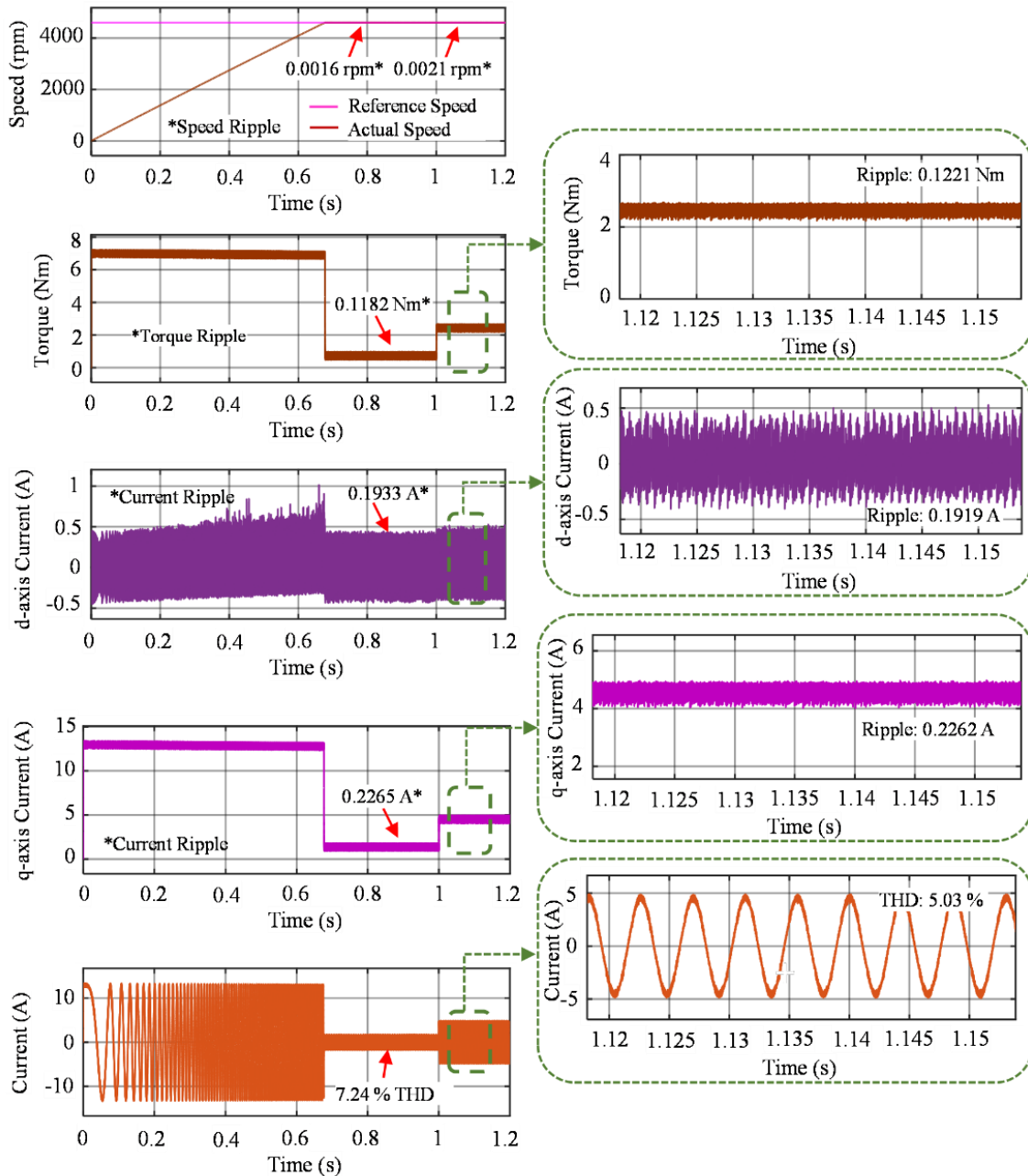


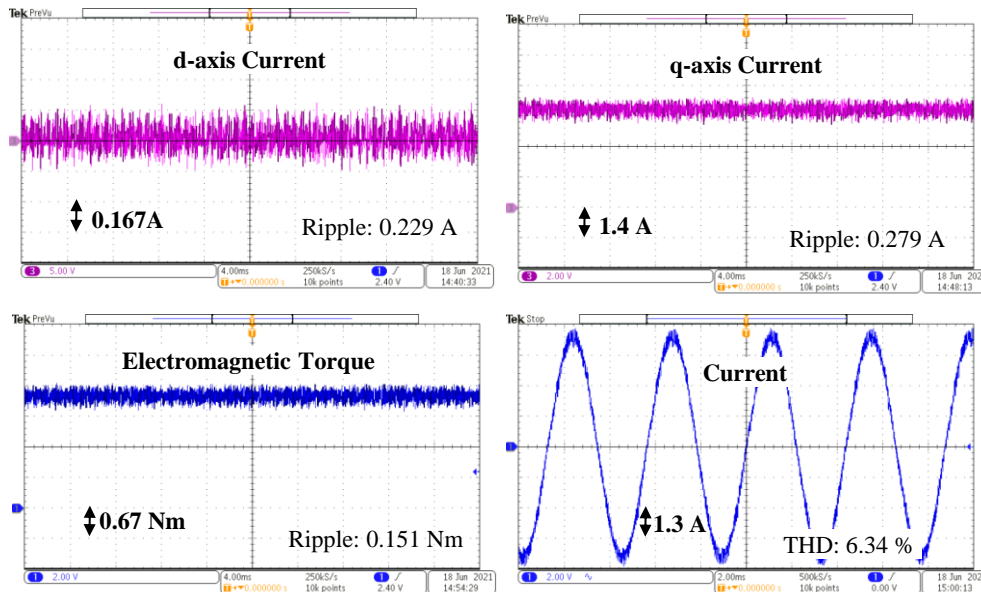**Figure 12.** *HTFC-based PMSM drive: Simulation results*

*Figure 13. HTFC-based PMSM drive: Experimental results at 4600 rpm*

The presence of ripple in the torque component of the current has resulted in the torque ripple of 0.12 Nm and 0.15 Nm in simulation and experimentation respectively. The current harmonics is 7.08% (refer to Figure 13). The d-q axes current ripples have distorted the waveform of the stator current and high total harmonic distortion (THD) has been observed.

### 5.2. MST Scheme

The drive performance of the MST-based drive at 4600 rpm is depicted in Figures 14-15. In this scheme, a 4-level hysteresis controller for $i_{qs}^e$ current error control is suggested. The dynamic response of the $i_{qs}^e$ error is decreased at the ±1 level, such that the inverter can be switched at the appropriate instant (±2 level of the hysteresis band). Thus, a reduction in the $i_{qs}^e$ ripple of 32.14% is observed with respect to the conventional HTFC scheme. The $i_{qs}^e$ current ripple (torque component) reduction, has resulted in the torque ripple minimization of about 27%.
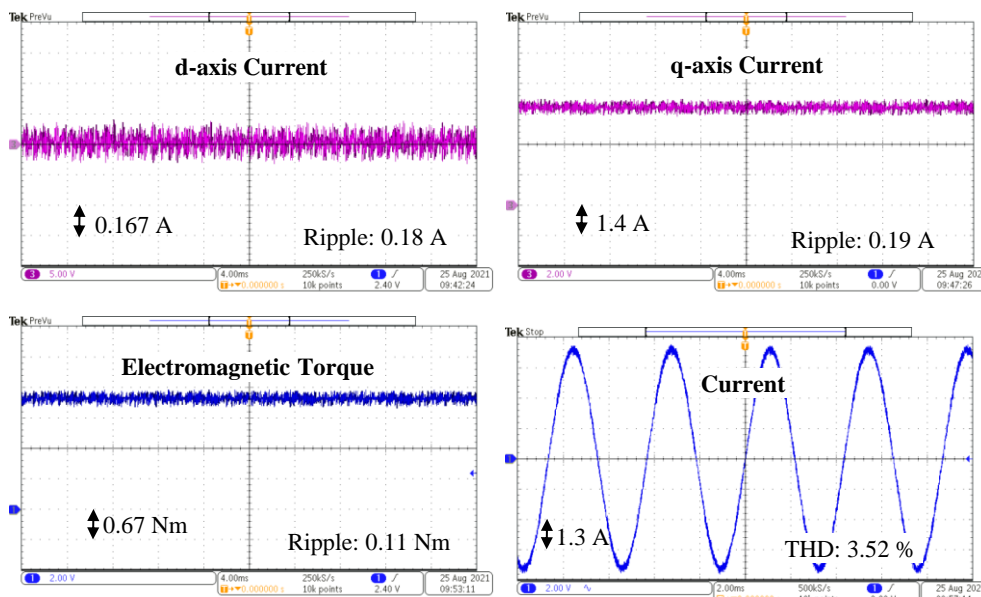


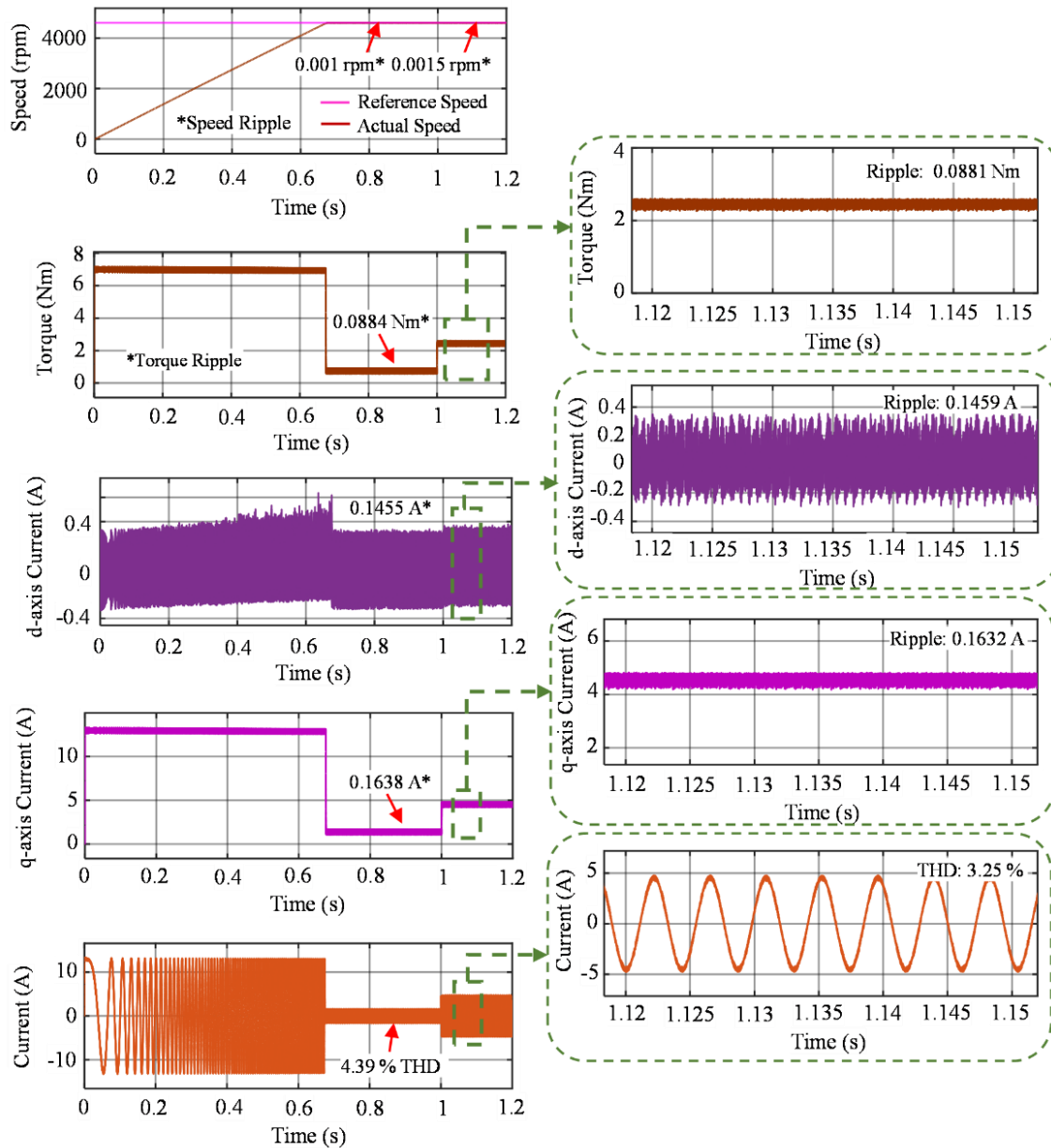*Figure 14. MST-based PMSM drive: Experimental results at 4600 rpm*

***Figure 15.** MST-based PMSM drive: Simulation results*

The $i_{ds}^e$ and $i_{qs}^e$ current characteristics have improved compared to the HTFC-based drive and a significant reduction of stator current harmonics of 44.48% is recorded. The switching frequency (average) of the MST-PMSM drive and HTFC-PMSM drive are 21.7 kHz and 25.7 kHz respectively. This reduction in the switching frequency (about 18%) is because of the proposed $i_{qs}^e$ current controller, which is a 4-level hysteresis control band in the MST scheme.

### 5.3. DRM Scheme

In the DRM drive, the control sampling time has been taken as 33μs. The DRM scheme-based PMSM drive has been simulated and validated experimentally at a drive speed of 4600 rpm and the results are presented in Figures 16 and 17, respectively.

The d-q axes current ripple is 0.13A and 0.15A respectively. The required duty ratio to achieve the minimum $i_{qs}^e$ current ripple is calculated in this scheme based on the $i_{qs}^e$ current response. Thus, a reduction in the $i_{qs}^e$ current ripple (compared to the HTFC scheme) of about 46% is achieved. The torque characteristics are influenced by the $i_{qs}^e$ current. With the reduction in the $i_{qs}^e$ ripple, a significant reduction in the electromagnetic torque ripple of 46.67% is observed. Similarly, minimized d-q axes current ripples have caused a significant decrease (64.35%) in the stator current harmonics.
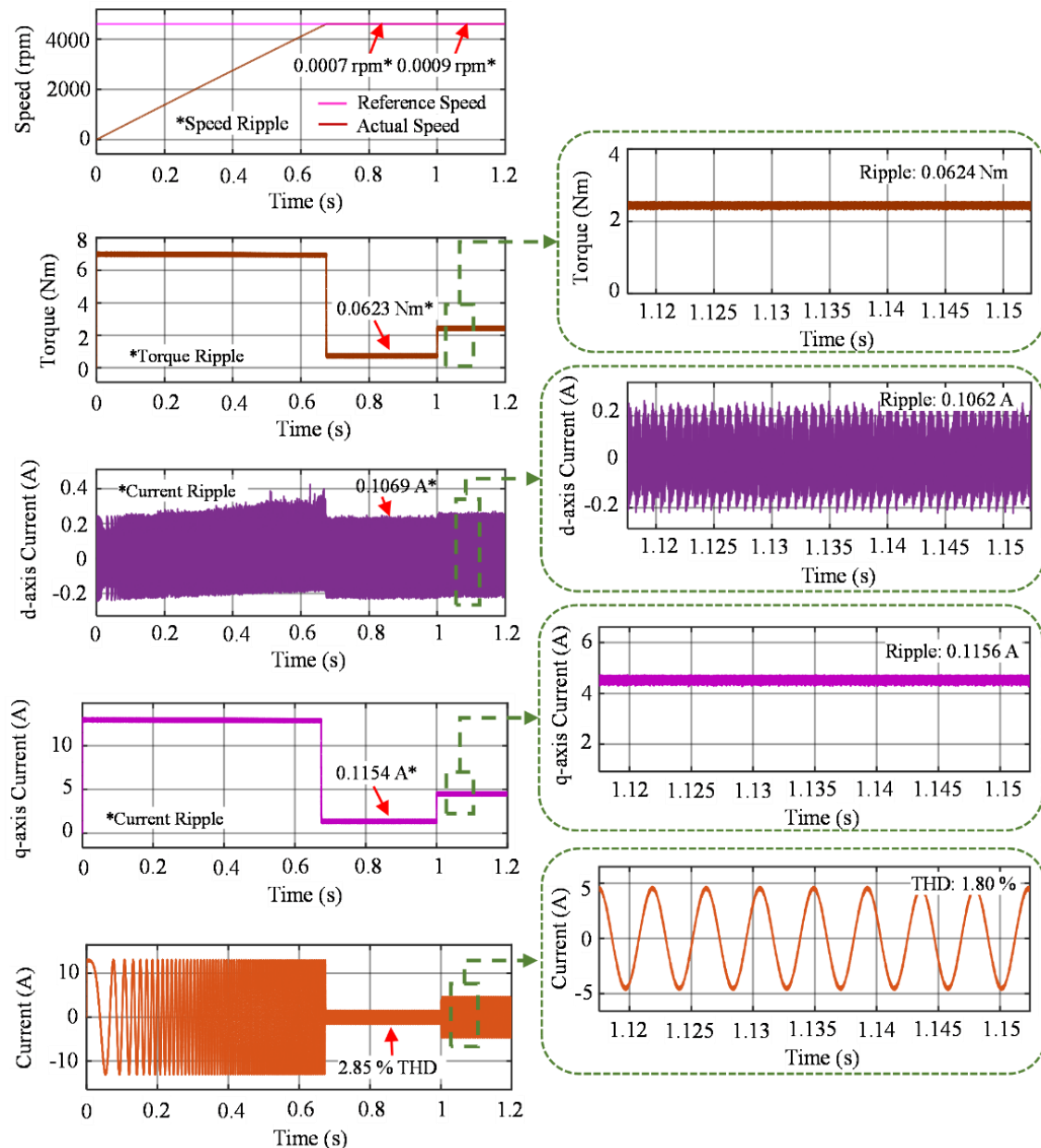


**Figure 16.** *DRM-based PMSM drive: Simulation results*

The PMSM drive performance at various drive speeds due to conventional and proposed HTFC schemes is presented in Figure 18. Performance comparisons of the MST scheme and DRM scheme with respect to the HTFC scheme are given in Tables 5 and 6, respectively (from Figures 12-17).
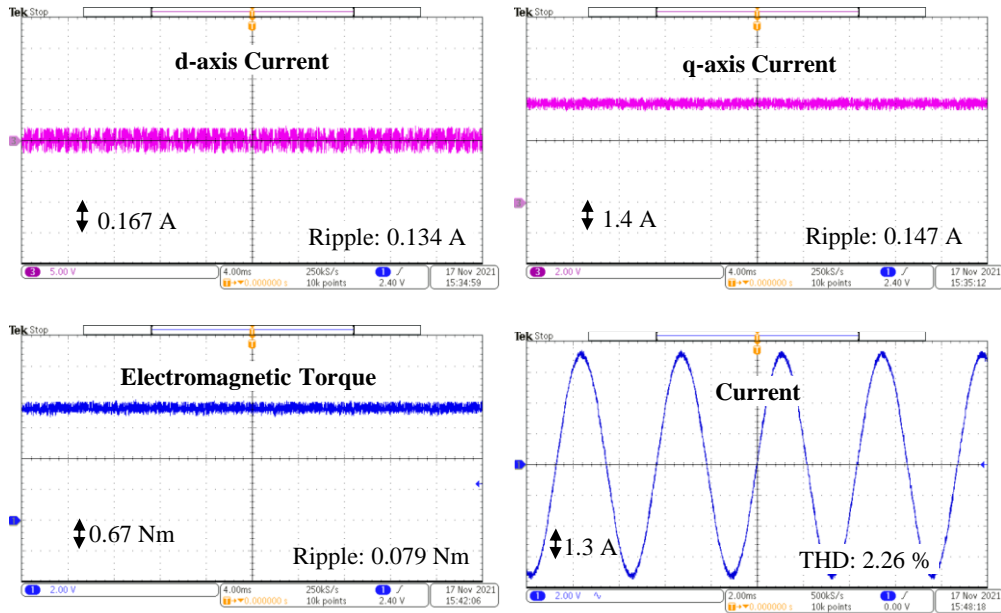
***Figure 17.*** *DRM-based PMSM drive: Experimental results at 4600 rpm*

***Table 5.*** *Performance comparison of 1kW PMSM motor drive at 4600 rpm: HTFC and MST schemes*

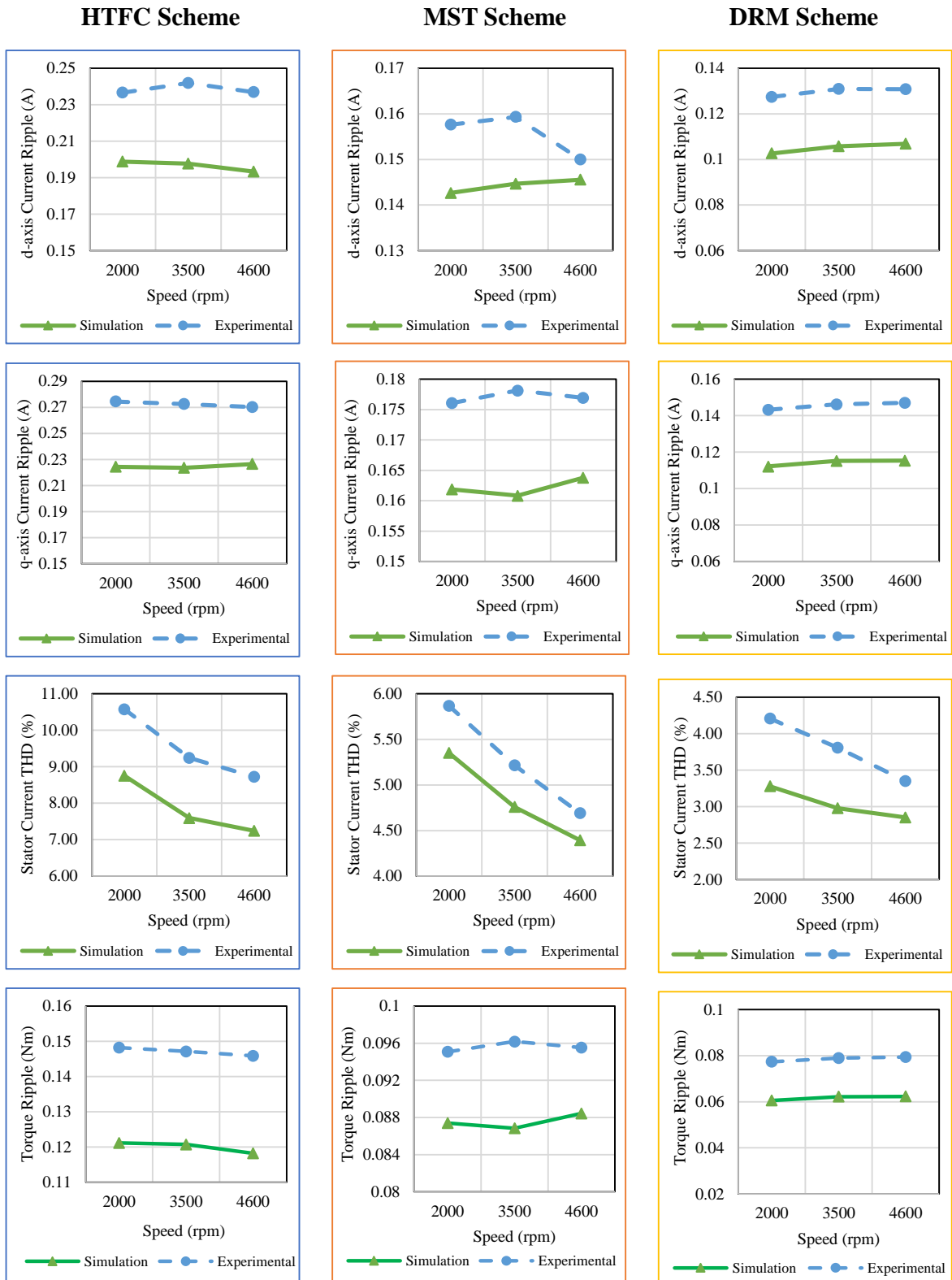| Parameter | HTFC scheme | MST scheme | Difference in % (with respect to HTFC scheme) | Inference |
|---|---|---|---|---|
| q-axis current ripple | Simulation result | | | The fast dynamic response of the q-axis current reduces its controllability within the two-level error hysteresis controller. But in the MST drive scheme, a 4-level hysteresis controller is suggested. The dynamics of the q-axis current error at the ±1 level is decreased, such that the inverter can be switched at an appropriate instant (±2 level of the hysteresis band). |
| | 0.23 A | 0.16 A | 30.43% ↓ | |
| | Experimental result | | | |
| | 0.28 A | 0.19 A | 32.14% ↓ | |
| Electromagnetic Torque ripple | Simulation result | | | The reduction in the torque component (q-axis current) ripple has minimized the electromagnetic torque ripple as well. |
| | 0.12 Nm | 0.088 Nm | 26.67% ↓ | |
| | Experimental result | | | |
| | 0.15 Nm | 0.11 Nm | 26.67% ↓ | |
| d-axis current ripple | Simulation result | | | The application of the intermediary voltage vector from the mutated switching table has caused a reduction in the d-axis current ripple. |
| | 0.19 A | 0.15 A | 21.05% ↓ | |
| | Experimental result | | | |
| | 0.23 A | 0.18 A | 21.74% ↓ | |
| Stator current harmonics | Simulation result | | | A significant drop in the stator current harmonics is observed because of the improved d- and q- axes current characteristics. |
| | 5.03% | 3.25% | 35.38% ↓ | |
| | Experimental result | | | |
| | 6.34% | 3.52% | 44.48% ↓ | |

***Figure 18.*** *PMSM drive performance at 0.5 Nm torque at various speeds*

***Table 6.** Performance comparison of 1kW PMSM motor drive at 4600 rpm: HTFC and DRM schemes*

| Parameter | HTFC scheme | DRM scheme | Difference in % (with respect to HTFC scheme) | Inference |
|---|---|---|---|---|
| q-axis current ripple | Simulation result | | | In the DRM scheme, the required duty ratio to achieve the minimum q-axis current ripple is calculated from the q-axis current response. |
| | 0.23 A | 0.12 A | 47.82% ↓ | |
| | Experimental result | | | |
| | 0.28 A | 0.15 A | 46.43% ↓ | |
| Electromagnetic Torque ripple | Simulation result | | | With the reduction in the q-axis current ripple, a significant reduction in the electromagnetic torque ripple is also observed. |
| | 0.12 Nm | 0.06 Nm | 50% ↓ | |
| | Experimental result | | | |
| | 0.15 Nm | 0.08 Nm | 46.67% ↓ | |
| d-axis current ripple | Simulation result | | | In the DRM scheme, the control voltage vectors needed to control the dq-axes current errors are selected from the switching table. The switching of the control voltage vector at the predicted duty ratio has also resulted in the d-axis current ripple. |
| | 0.19 A | 0.11 A | 42.1% ↓ | |
| | Experimental result | | | |
| | 0.23 A | 0.13 A | 43.48% ↓ | |
| Stator current harmonics | Simulation result | | | The reduction in the d-q axes' current ripples has caused a significant reduction in the stator current harmonics. |
| | 5.03% | 1.80% | 64.21% ↓ | |
| | Experimental result | | | |
| | 6.34% | 2.26% | 64.35% ↓ | |

## 5.4. Thermal Performance

The stator current characteristics such as harmonics and RMS current, and the switching frequency influence the loss in the inverter module of the drive [60-65]. In this section, the temperature variation observed in the inverter drive due to HTFC, MST, and DRM schemes is discussed. The fundamental power loss (average) calculation equations for an IGBT and diode in an average switching period ($1/f_{sw}$) are tabulated in Table 7 [1, 60]. It can be observed that the losses in the power inverter mainly occur due to the load current and the switching frequency. At 4600 rpm, the RMS current, harmonics, and switching frequency observed are depicted in Figure 19.

***Table 7.** Inverter PCB thermal images – HTFC, MST, and DRM schemes*

| Power Loss (W) | | IGBT | Diode |
|---|---|---|---|
| Conduction, $P_{con}$ | | $P_{con} = I_L V_{CE(sat)}$ | $P_{con.=} I_L V_F$ |
| Switching, $P_{sw}$ | Turn-ON | $P_{sw\,(on).=} f_{sw} E_{on}$ | - |
| | Turn-OFF | $P_{sw\,(off).=} f_{sw} E_{off}$ | $P_{sw.=} f_{sw} E_{rec}$ (during reverse recovery) |

$I_L$ = load current; $V_{CE(sat)}$ = On-state voltage of the IGBT; $V_F$ = On-state voltage of the diode; $E_{on}$ and $E_{off}$ = Turn ON and Turn OFF switching energy of the IGBT; $E_{rec}$ = Turn OFF (reverse recovery) switching energy of the diode

The thermal graphs of the inverter are recorded after the drive run time of 60 min using a thermal imaging camera – FLIR E75. The temperature contour of the inverter PCB due to HTFC, MST, and DRM schemes at rated drive conditions is presented in Table 8. From the results, it can be inferred that the minimization of the current ripples also causes temperature variation in the inverter drive. Since the DRM scheme has improved d-q axis current characteristics (minimum current ripple and harmonics), it records a maximum temperature of 48.3ºC in the power inverter which is 1.7ºC lower than the HTFC scheme.
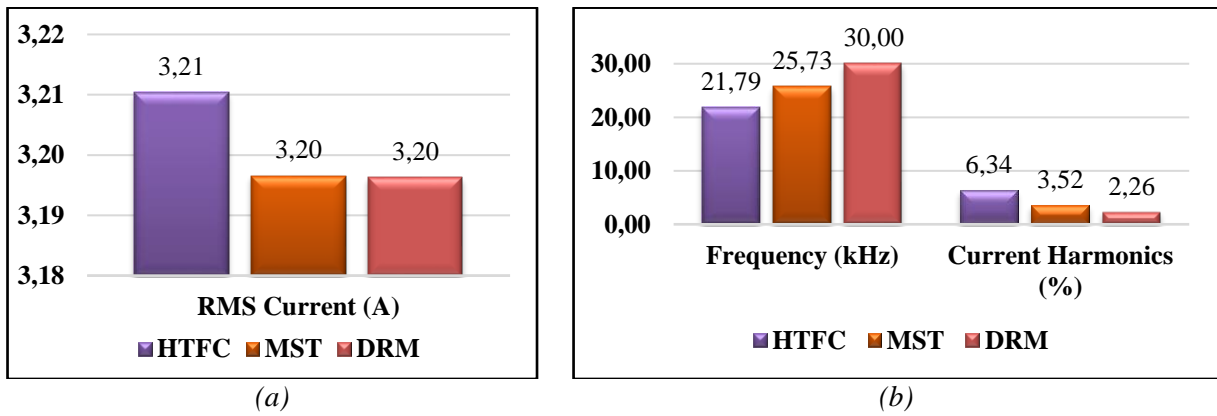
**Figure 19.** *(a) RMS current, (b) harmonics, and switching frequency of the HTFC, MST, and DRM based PMSM drives at 4600 rpm*

**Table 8.** *Inverter PCB thermal images – HTFC, MST, and DRM schemes*

| Scheme | Front View | Back View |
|---|---|---|
| HTFC |  |  |
| MST |  |  |
| DRM |  |  |

## 6. RESULTS AND DISCUSSION

In this paper, the HTFC scheme has been introduced for the PMSM drive. The performance of the HTFC-based PMSM drive has been analysed in simulation and also validated experimentally. Based on the results obtained it has been observed that the DTC-like control structure of the conventional scheme (HTFC) causes ripples in the dq currents (0.23 A and 0.28 A respectively) and it also influences the torque and current harmonics.

To overcome the above drawbacks, two schemes have been proposed. (1) MST scheme, (2) DRM scheme. It has been observed that these schemes reduced the ripples in the current components significantly compared to the HTFC scheme. The current ripple also impacts the losses occurring in the power inverter of the drive. During testing, it has been observed that the minimization of current ripples also reduces the temperature of the inverter for the proposed schemes. In the PMSM drive, variation in the PMSM parameters occurs due to the thermal impact and ageing. This causes errors in the control parameter estimation such as electromagnetic torque, flux, and duty ratio. The inverter non-linearity also causes errors in the drive control. To overcome these drawbacks, parameter error compensation techniques such as using Kalman Filter, least-square estimation, etc. can be applied.

## CONFLICTS OF INTEREST

No conflict of interest was declared by the authors.

### *Nomenclature*

| | |
|---|---|
| $i_{ds}^e$  $i_{qs}^e$ | d-axis and q-axis stator currents (A) |
| $v_{ds}^e$  $v_{qs}^e$ | d-axis and q-axis stator voltages (V) |
| $i_{as}, i_{bs}, i_{cs}$ or $i_{abcs}$ | Phase currents of the motor (A) |
| $I_s$ | Resultant phase current of the motor (A) |
| $\psi_{ds}^e$  $\psi_{qs}^e$  $\psi_f$ | d-axis, q-axis flux linkages and magnet flux linkage of the motor (Wb) |
| $L_d$  $L_q$ | d-axis and q-axis inductances (H) |
| $T_e$  $\delta$ | Electromagnetic torque (Nm) and load angle (rad.) |
| $P$ | Number of the magnetic poles in the motor |
| $\omega_e$  $\theta_e$ | Electrical angular speed in rad./sec and rotor position in electrical rad. |

| | |
|---|---|
| $v_{dc}$ | DC-link voltage (V) |
| $H_{ids}$  $H_{iqs}$ | Hysteresis controller output status |
| $+HB_{ids}$  $-HB_{ids}$ | Upper band and lower band limits of the d-axis current error hysteresis band (A) |
| $+HB_{iqs}$  $-HB_{iqs}$ | Upper band and lower band limits of the q-axis current error hysteresis band (A) |
| $S_1 - S_{24}$ | Sectors of the d-q space |
| $\dfrac{di_{qs}^e}{dt}$ | Rate of change of the q-axis current |
| $V_1 - V_6$ | Voltage vector of the inverter |
| $t_s$  $t_{cs}$ | Inverter voltage vector switching time (s) and control sampling time (s) |

## REFERENCES

[1]    Bose, B. K., "Modern Power Electronics and AC Drives", PHI Learning Pvt. Ltd, (2013).

[2]    Krishnan, R., "Electric Motor Drives: Modeling, Analysis and Control", Prentice Hall, (2002).

[3]    Vas, P., "Sensorless Vector and Direct Torque Control", Oxford University Press, (1998).

[4] Abu-Rub, H., Iqbal, A., Guzinski, J., "High Performance Control of AC Drives with Matlab/Simulink", John Wiley & Sons, (2021).

[5] Takahashi, I., Noguchi, T., "A new quick-response and high-efficiency control strategy of an induction motor", IEEE Transactions on Industry Applications, IA-22(5): 820-827, (1986).

[6] Takahashi, I., Ohmori, Y., "High-performance direct torque control of an induction motor", IEEE Transactions on Industry Applications, 25(2): 257-264, (1989).

[7] Zhong, L., Rahman, M.F., Hu, W.Y., Lim, K.W., "Analysis of direct torque control in permanent magnet synchronous motor drives", IEEE Transactions on Power Electronics, 12(3): 528-536, (1997).

[8] Casadei, D., Profumo, F., Serra, G., Tani, A., "FOC and DTC: two viable schemes for induction motors torque control", IEEE Transactions on Power Electronics, 17(5): 779-787, (2002).

[9] Kumar, R.H., Iqbal, A., Lenin, N.C., "Review of recent advancements of direct torque control in induction motor drives – a decade of progress", IET Power Electronics, 11: 1-15, (2018).

[10] Lemma, B.D., Pradabane, S., "Control of PMSM drive using lookup table based compensated duty ratio optimized direct torque control (DTC)", IEEE Access, 11: 19863-19875, (2023).

[11] Blaschke, F., "A new method for the structural decoupling of AC induction machines", in Conf. Rec. IFAC 1971, 1: 1-15, (1971).

[12] Pillay, P., Krishnan, R., "Modeling, simulation, and analysis of permanent-magnet motor drives. I. The permanent-magnet synchronous motor drive", IEEE Transactions on Industry Applications, 25(2): 265-273, (1989).

[13] Kazmierkowski, M.P., Malesani, L., "Current control techniques for three-phase voltage-source PWM converters: a survey", IEEE Transactions on Industrial Electronics, 45(5): 691-703, (1998).

[14] Holmes, D.G., Lipo, T.A., McGrath, B.P., Kong, W.Y., "Optimized design of stationary frame three phase AC current regulators", IEEE Transactions on Power Electronics, 24(11): 2417-2426, (2009).

[15] Ullah, K., Guzinski, J., Mirza, A.F., "Critical review on robust speed control techniques for permanent magnet synchronous motor (PMSM) speed regulation", Energies, 15(3): 1235-1247, (2022).

[16] Zordan, M., Vas, P., Rashed, M., Ng, C.H., Bolognani, S., Zigliotto, M., "Field-weakening in high-performance PMSM drives", COMPEL-The İnternational Journal for Computation and Mathematics in Electrical and Electronic Engineering, 21(2): 338-354, (2002).

[17] Kazmierkowski, M.P., Sulkowski, W., "A novel vector control scheme for transistor PWM inverter-fed induction motor drive", IEEE Transactions on Industrial Electronics, 38(1): 41-47, (1991).

[18] Kazmierkowski, M.P., Dzieniakowski, M.A., Sulkowski, W., "Novel space vector based current controllers for PWM-inverters", IEEE Transactions on Power Electronics, 6(1): 158-166, (1991).

[19] Ravi, H.K., Natesan Chokkalingam, L., "Current ripple reduction to improve electromagnetic torque and flux characteristics in AC drives", International Journal of Electronics, 109(8): 1421-1442, (2022).

[20] Mohd Zaihidee, F., Mekhilef, S., Mubin, M., "Robust speed control of PMSM using sliding mode control (SMC)—A review", Energies, 12(9): 1669-1695, (2019).

[21]   Wang, X., Steve Suh, C.A., "Nonlinear time–frequency control based FOC for permanent magnet synchronous motors", International Journal of Dynamics and Control, 9: 179-189, (2021).

[22]   Rafaq, M.S., Midgley, W., Thomas Steffen, T., "Review of the state of the art of torque ripple minimization techniques for permanent magnet synchronous motors", IEEE Transactions on Industrial Informatics, 1-13, (2023).

[23]   van der Broeck, H.W., Skudelny, H.-C., Stanke, G.V., "Analysis and realization of a pulsewidth modulator based on voltage space vectors", IEEE Transactions on Industry Applications, 24(1): 142-150, (1988).

[24]   Zmood, D.N., Holmes, D.G., "Stationary frame current regulation of PWM inverters with zero steady-state error", IEEE Transactions on Power Electronics, 18(3): 814-822, (2003).

[25]   Holmes, D.G., Lipo, T.A., McGrath, B.P., Kong, W.Y., "Optimized design of stationary frame three phase AC current regulators", IEEE Transactions on Power Electronics, 24(11): 2417-2426, (2009).

[26]   Rowan, T.M., Kerkman, R.J., "A new synchronous current regulator and an analysis of current-regulated PWM inverters", IEEE Transactions on Industry Applications, IA-22(4): 678-690, (1986).

[27]   Sepe, R.B., Lang, J.H., "Inverter nonlinearities and discrete-time vector current control", IEEE Transactions on Industry Applications, 30(1): 62-70, (1986).

[28]   Singh, G.K., Singh, D.K.P., Nam, K., Lim, S.K., "A simple indirect field-oriented control scheme for multiconverter-fed induction motor", IEEE Transactions on Industrial Electronics, 52(6): 1653-1659, (2005).

[29]   Wang, K., Li, Y., Ge, Q., Shi, L., "An improved indirect field-oriented control scheme for linear induction motor traction drives", IEEE Transactions on Industrial Electronics, 65(12): 9928-9937, (2018).

[30]   Domínguez, J.R., Dueñas, I., Ortega-Cisneros, S., "Discrete-time modeling and control based on field orientation for induction motors", IEEE Transactions on Power Electronics, 35(8): 8779-8793, (2020).

[31]   Lorenz, R.D., Lawson, D.B., "Performance of feedforward current regulators for field-oriented induction machine controllers", IEEE Transactions on Industry Applications, IA-23(4): 597-602, (1987).

[32]   Dong-Choon Lee, Sul, S.-K., Min-Ho Park., "High performance current regulator for a field-oriented controlled induction motor drive", IEEE Transactions on Industry Applications, 30(5): 1247-1257, (1994).

[33]   Kawabata, Y., Kawakami, T., Sasakura, Y., Ejiogu, E.C., Kawabata, T., "New design method of decoupling control system for vector controlled induction motor", IEEE Transactions on Power Electronics, 19(1): 1-9, (2004).

[34]   Bozorgi, A.M., Farasat, M., Jafarishiadeh, S., "Model predictive current control of surface-mounted permanent magnet synchronous motor with low torque and current ripple", IET Power Electronics, 10(10): 1120-1128, (2017).

[35]   Qu, J., Jatskevich, J., Zhang, C., Zhang, S., "Improved multiple vector model predictive torque control of permanent magnet synchronous motor for reducing torque ripple", IET Electric Power Applications, 15: 681-695, (2021).

[36]  M L, P, Eshwar, K., Thippiripati, V.K., "A modified duty-modulated predictive current control for permanent magnet synchronous motor drive", IET Electric Power Applications, 15: 25-38, (2021).

[37]  Fan, S., Zhang, Y., Jin, J., Wang, X., Tong, C., "Deadbeat predictive current control of PMSM drives with an adaptive flux-weakening controller", IET Power Electronics, 15: 753-763, (2022).

[38]  Brod, D.M., Novotny, D.W., "Current control of VSI-PWM inverters", IEEE Transactions on Industry Applications, IA-21(3): 562-570, (1985).

[39]  Huang, C.-Y., Wei, C.-P., Yu, J.-T., Hu, Y.-J., "Torque and current control of induction motor drives for inverter switching frequency reduction", IEEE Transactions on Industrial Electronics, 52(5): 1364-1371, (2005).

[40]  Chang, T.-Y., Pan, C.-T., "A practical vector control algorithm for /spl mu/-based induction motor drives using a new space vector current controller", IEEE Transactions on Industrial Electronics, 41(1): 97-103, (1994).

[41]  Pan, C.-T., Chang, T.-Y., "An improved hysteresis current controller for reducing switching frequency", IEEE Transactions on Power Electronics, 9(1): 97-104, (1994).

[42]  Liu, Y.-H., Chen, C.-L., Tu, R.-J., "A novel space-vector current regulation scheme for a field-oriented-controlled induction motor drive", IEEE Transactions on Industrial Electronics, 45(5): 730-737, (1998).

[43]  Kwon, B.-H., Kim, T.-W., Youm, J.-H., "A novel SVM-based hysteresis current controller", IEEE Transactions on Power Electronics, 13(2): 297-307, (1998).

[44]  Vaez-Zadeh, S., Jalali, E., "Combined vector control and direct torque control method for high performance induction motor drives", Energy Conversion and Management, 48(12): 3095-3101, (2007).

[45]  Karimi, H., Vaez-Zadeh, S., Rajaei Salmasi, F., "Combined vector and direct thrust control of linear induction motors with end effect compensation", IEEE Transactions on Energy Conversion, 31(1): 196-205, (2016).

[46]  Kawamura, A., Hoft, R., "Instantaneous feedback controlled PWM inverter with adaptive hysteresis", IEEE Transactions on Industry Applications, IA-20(4): 769-775, (1984).

[47]  Bose, B.K., "An adaptive hysteresis-band current control technique of a voltage-fed PWM inverter for machine drive system", IEEE Transactions on Industrial Electronics, 37(5): 402-408, (1990).

[48]  Holtz, J., Beyer, B., "The trajectory tracking approach-a new method for minimum distortion PWM in dynamic high-power drives", IEEE Transactions on Industry Applications, 30(4): 1048-1057, (1994).

[49]  Zhang, J., Yang, H., Wang, T., Li Li, Dorrell, D. G., Dah-Chuan Lu, D., "Field-oriented control based on hysteresis band current controller for a permanent magnet synchronous motor driven by a direct matrix converter", IET Power Electronics, 11(7): 1277-1285, (2018).

[50]  Holtz, J., Beyer, B., "Fast current trajectory tracking control based on synchronous optimal pulsewidth modulation", IEEE Transactions on Industry Applications, 31(5): 1110-1120, (1995).

[51]    Öztürk, N., Çelik, E., "An Educational Tool for the Genetic Algorithm-Based Fuzzy Logic Controller of a Permanent Magnet Synchronous Motor Drive", International Journal of Electrical Engineering & Education, 51(3): 218-231, (2014).

[52]    Wang, Z., Yang, M., Gao, L., Wang, Z., Zhang, G., Wang, H., Xin Gu., "Deadbeat predictive current control of permanent magnet synchronous motor based on variable step-size adaline neural network parameter identification", IET Electric Power Applications, 14(11): 2007-2015, (2020).

[53]    Öztürk, N., Çelik, E., "Speed control of permanent magnet synchronous motors using fuzzy controller based on genetic algorithms", International Journal of Electrical Power & Energy Systems, 43(1): 889-898, (2012).

[54]    Çelik, E., Dalcali, A., Öztürk, N., Canbaz, R., "An adaptive PI controller schema based on fuzzy logic controller for speed control of permanent magnet synchronous motors", 4th International Conference on Power Engineering, Energy and Electrical Drives, Istanbul, Turkey, 715-720, (2013).

[55]    Masiala, M., Vafakhah, B., Salmon, J., Knight, A.M., "Fuzzy self-tuning speed control of an indirect field-oriented control induction motor drive", IEEE Transactions on Industry Applications, 44(6): 1732-1740, (2008)

[56]    Khiabani, A.G., Heydari, A., "Optimal torque control of permanent magnet synchronous motors using adaptive dynamic programming", IET Power Electronics, 13(12): 2442-2449, (2020).

[57]    Hannan, M.A., Ali, J.A., Mohamed, A., Amirulddin, U.A.U., Tan, N.M.L., Uddin, M.N., "Quantum-behaved lightning search algorithm to improve indirect field-oriented fuzzy-PI control for IM drive", IEEE Transactions on Industry Applications, 54(4): 3793-3805, (2018).

[58]    Farah, N., Talib, Md.H.N., Mohd Shah, N.S., Abdullah, Q., Ibrahim, Z., Lazi, J. B. M., Jidin, A., "A novel self-tuning fuzzy logic controller based induction motor drive system: an experimental approach", IEEE Access, 7: 68172-68184, (2019).

[59]    Jun-Koo Kang, Sul, S.-K., "New direct torque control of induction motor for minimum torque ripple and constant switching frequency", IEEE Transactions on Industry Applications, 35(5): 1076-1082, (1999).

[60]    Kim, S.C., "Thermal performance of motor and inverter in an integrated starter generator system for a hybrid electric vehicle", Energies, 6(11): 6102-6119, (2013).

[61]    Chen, K., Ahmed, S., Maly, D., Parkhill, S., Flett, F., "Comparison of thermal performance of different power electronic stack constructions", SAE Transactions, 111(7): 772-776, (2002).

[62]    Lemmens, J., Vanassche, P., Driesen, J., "Optimal control of traction motor drives under electrothermal constraints", IEEE Journal of Emerging and Selected Topics in Power Electronics, 2(2): 249-263, (2014).

[63]    Franke, T., "Current and temperature distribution in multi-chip modules under inverter operation", in Proceedings of the 8th European Conference on Power Electronics and Applications, Lausanne, Switzerland, (1999).

[64]    Carubelli, S., Khatir, Z., "Experimental validation of a thermal modelling method dedicated to multichip power modules in operating conditions", Microelectronics Journal, 34(12): 1143-1151, (2003).

[65] Zhang, S., Wang, C., Zhong, H., Zhao, Z., Feng, J., Wu, Q., Wu, J., "Study on the temperature distribution of motor and inverter in an electric scroll compressor for vehicle air conditioning under refrigeration conditions", International Journal of Refrigeration, 154: 111-124, (2023).